



Retrieval of large volcanic SO₂ columns from the Aura Ozone Monitoring Instrument: Comparison and limitations

Kai Yang,¹ Nickolay A. Krotkov,¹ Arlin J. Krueger,² Simon A. Carn,² Pawan K. Bhartia,³ and Pieter F. Levelt⁴

Received 15 April 2007; revised 16 July 2007; accepted 10 August 2007; published 29 November 2007.

[1] To improve global measurements of atmospheric sulfur dioxide (SO₂), we have developed a new technique, called the linear fit (LF) algorithm, which uses the radiance measurements from the Ozone Monitoring Instrument (OMI) at a few discrete ultraviolet wavelengths to derive SO₂, ozone, and effective reflectivity simultaneously. We have also developed a sliding median residual correction method for removing both the along- and cross-track biases from the retrieval results. The achieved internal consistencies among the LF-retrieved geophysical parameters clearly demonstrate the success of this technique. Comparison with the results from the Band Residual Difference technique has also illustrated the drastic improvements of this new technique at high SO₂ loading conditions. We have constructed an error equation and derived the averaging kernel to characterize the LF retrieval and understand its limitations. Detailed error analysis has focused on the impacts of the SO₂ column amounts and their vertical distributions on the retrieval results. The LF algorithm is robust and fast; therefore it is suitable for near real-time application in aviation hazards and volcanic eruption warnings. Very large SO₂ loadings (>100 DU) require an off-line iterative solution of the LF equations to reduce the retrieval errors. Both the LF and sliding median techniques are very general so that they can be applied to measurements from other backscattered ultraviolet instruments, including the series of Total Ozone Mapping Spectrometer (TOMS) missions, thereby offering the capability to update the TOMS long-term record to maintain consistency with its OMI extension.

Citation: Yang, K., N. A. Krotkov, A. J. Krueger, S. A. Carn, P. K. Bhartia, and P. F. Levelt (2007), Retrieval of large volcanic SO₂ columns from the Aura Ozone Monitoring Instrument: Comparison and limitations, *J. Geophys. Res.*, *112*, D24S43, doi:10.1029/2007JD008825.

1. Introduction

[2] Major contributions to sulfur dioxide (SO₂) in the atmosphere come from both anthropogenic activities and natural phenomena, which include combustion of fossil fuels, smelting of ores, burning of biomass, oxidation of dimethylsulphate (DMS) over oceans, and degassing and eruptions of volcanoes. The change in the abundance of atmospheric SO₂ and its spatial and temporal distribution can have significant impacts on the environment and climate. Remote sensing instruments measuring solar backscattered ultraviolet (BUV) radiation on board satellite platforms have played critical role in monitoring and

quantifying these SO₂ emissions. The most notable of these instruments was the Total Ozone Mapping Spectrometer (TOMS) [Krueger, 1983; McPeters *et al.*, 1998], which provided a unique and near-continuous long-term (from 1978 to 2006) data record of volcanic SO₂ [Krueger *et al.*, 2000; Carn *et al.*, 2003; A. J. Krueger *et al.*, El Chichon: The genesis of volcanic sulfur dioxide monitoring from space, submitted to *Journal of Volcanology and Geothermal Research*, 2007] and ash [Krotkov *et al.*, 1997, 1999a, 1999b; Seftor *et al.*, 1997] emissions. The Dutch-Finnish Ozone Monitoring Instrument (OMI) [Levelt *et al.*, 2006], launched on the EOS/Aura platform in July 2004, is continuing and expanding these records that are invaluable to both atmospheric scientists and volcanologists [Krotkov *et al.*, 2006, 2007; Carn *et al.*, 2007a, 2007b]. OMI data are also of considerable value for aviation safety through near real-time processing for the detection of volcanic SO₂ and ash clouds.

[3] OMI has combined the hyperspectral measurements similar to those made by the Global Ozone Monitoring Experiment (GOME) [Burrows *et al.*, 1999] and the Scanning Imaging Absorption Spectrometer for Atmospheric

¹Goddard Earth Sciences and Technology Center, University of Maryland Baltimore County, Baltimore, Maryland, USA.

²Joint Center for Earth Systems Technology, University of Maryland Baltimore County, Baltimore, Maryland, USA.

³Laboratory for Atmospheres, NASA Goddard Space Flight Center, Greenbelt, Maryland, USA.

⁴Royal Dutch Meteorological Institute, De Bilt, Netherlands.

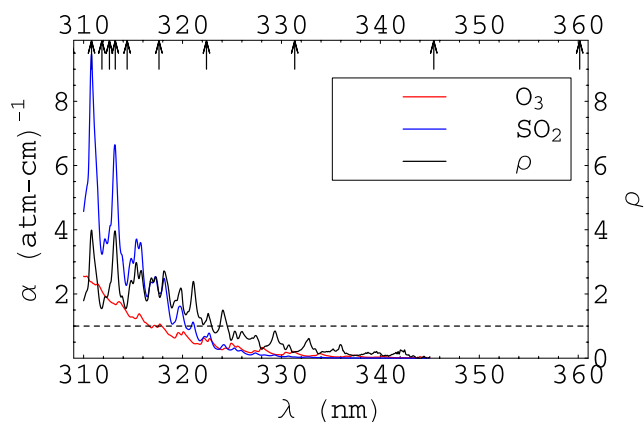


Figure 1. Absorption coefficients (α) of SO₂ and O₃ and their ratio (ρ), SO₂ to O₃, as a function of wavelength, indicating that a SO₂ molecule can have 4 times stronger absorption than an O₃ molecule. The positions indicated by the arrows are the central wavelengths of the OMTO3 bands used in the algorithm. These 10 central wavelengths are 310.80, 311.85, 312.61, 313.20, 314.40, 317.62, 322.42, 331.34, 345.40, and 360.15 nm.

Chartography (SCIAMACHY) [Bovensmann *et al.*, 1999] with improved viewing capabilities, including daily contiguous global coverage with a high spatial resolution not achieved by any of its predecessors. OMI accomplishes this by the use of two-dimensional charge coupled device (CCD) detectors to measure backscattered radiances in spectral and spatial dimensions simultaneously, covering ultraviolet (UV) (270–365 nm) and visible (365–500 nm) ranges at high spectral sampling and resolution with a swath width of 2600 km at a nadir spatial resolution of 13 km \times 24 km. Having all these advanced characteristics, OMI provides an unprecedented measurement sensitivity to a number of atmospheric trace gases, including SO₂, which is the subject of the current study.

[4] Over the years a number of algorithms have been developed for retrieval of SO₂ from BUUV measurements in various parts of the spectral region between 310 and 340 nm. Like ozone, SO₂ has significant absorption structures in this region (see Figure 1). The typical vertical column density of SO₂ in the atmosphere (mostly in the boundary layer) is too small to have measurable impacts on the BUUV radiances. However, localized enhancements of SO₂, either from volcanic emissions or anthropogenic pollution, can produce noticeable absorption effects, sometimes comparable to or even exceeding those due to ozone in the atmosphere. The challenge of SO₂ retrieval is to distinguish its absorption effects from those of ozone.

[5] For the series of TOMS instruments, which measured backscattered radiances at six discrete UV wavelength bands, the Krueger-Kerr algorithm [Krueger *et al.*, 1995; Gurevich and Krueger, 1997] was used for the retrieval of its entire record. This algorithm derived ozone and SO₂ vertical column amounts from the direct inversion of a set of linear equations between the measurements and absorption and scattering optical thickness at four wavelength bands. It provided reasonable SO₂ values for large volcanic clouds,

but suffered from unrealistic uncertainty in the background area because the equation was sometimes ill conditioned, leading to a solution that was highly sensitive to measurement noises.

[6] For GOME and SCIAMACHY, the standard Differential Optical Absorption Spectroscopy (DOAS) fitting technique has been applied to the measurements in the 315–327 nm wavelength window to derive slant column amounts of SO₂ along the viewing-illumination path [Richter *et al.*, 2006; Thomas *et al.*, 2005; Khokhar *et al.*, 2005; Bramstedt *et al.*, 2004; Eisinger and Burrows, 1998]. These slant columns are then converted into vertical columns using air mass factors (AMF) computed at a single wavelength. Retrievals from GOME and SCIAMACHY have demonstrated that a much improved SO₂ detection limit has been achieved by frequent observations of anthropogenic SO₂ in heavily polluted regions [Khokhar *et al.*, 2005; Richter *et al.*, 2006]. However the traditional DOAS algorithm, well suited for retrieval of absorbers when they are optically thin, may lose its accuracy if a single-wavelength AMF is used for SO₂ when column amounts become large. Recent advances in the DOAS technique, like the empirical AMF approach developed for the OMI DOAS ozone product [Veeffkind *et al.*, 2006], could alleviate this problem by accounting for wavelength-dependent effects on the AMF induced by strong SO₂ absorption.

[7] For OMI, we have developed a technique called the band residual difference (BRD) algorithm that uses only four wavelength bands in the UV2 (310–365 nm) region [Krotkov *et al.*, 2006]. These bands are centered at the local minima and maxima of the SO₂ absorption cross section (see Figure 1) between 310.8 and 314.4 nm. This selection enables the BRD technique to take advantage of the large differential absorption of the three pairs formed by the adjacent bands, thereby maximizing the detection sensitivity to small SO₂ column amounts. Doing so, however, makes this technique unsuitable for situations with large SO₂ loadings, when the band residual differences of these pairs show nonlinear and nonmonotonic responses to SO₂ increments.

[8] In an effort to improve the retrieval of SO₂ from BUUV measurements, especially for the cases with high SO₂ column amounts, we introduce a more generalized technique called the linear fit (LF) algorithm for application to OMI SO₂ retrieval. The LF algorithm is based on the spectral fitting technique [Joiner and Bhartia, 1997] developed for ozone retrieval from the full spectral measurements of the Solar Backscattered Ultraviolet (SBUV) instrument. This fitting technique was further developed [Yang *et al.*, 2004] to combine with the TOMS-V8 retrieval [Bhartia and Wellemeyer, 2002; Wellemeyer *et al.*, 2004] and was applied to GOME measurements, and now it is adopted and extended to perform simultaneous retrieval of ozone, SO₂, and surface reflectivity using just a few discrete UV bands. Note that a similar algorithm, called the Weighting Function DOAS, has been developed by Buchwitz *et al.* [2000] and then applied by Coldewey-Egbers *et al.* [2005] to retrieve total column ozone from GOME measurements.

[9] This paper describes the LF algorithm and provides extensive analysis on the various error sources and their impacts on the SO₂ retrieval accuracy. Examples of retriev-

als from volcanic plumes observed by OMI under various conditions and comparisons with the BRD retrievals are presented. The limitations and future improvements of this technique are discussed.

2. Algorithm Description

2.1. Overview

[10] The BUUV radiance measurements I_m (normalized to the incoming solar irradiance) relate the geophysical parameters, consisting of vertical columns of ozone (Ω), SO₂ (Ξ), surface reflectivity (R), and others, via a radiative transfer model that calculates the top-of-the-atmosphere (TOA) radiances I . Taking the log of the measured and modeled radiances at a single wavelength band, their relation can be expressed as

$$\begin{aligned} \log_{10} I_m &= \log_{10} I(\Omega, \Xi, R) + \varepsilon \\ N_m &= N(\Omega, \Xi, R) + \varepsilon_T. \end{aligned} \quad (1)$$

where $N = -100 \log_{10} I$, and $\varepsilon_T = -100 * \varepsilon$, denotes the total error, a combination of measurement and model errors, for the band. N is a dimensionless quantity, usually referred to as N value.

[11] In general, TOA radiances are a function of the vertical profiles of the absorbers, which are ozone and SO₂ in our study. However, because of the weak profile shape effects under most observing conditions for wavelengths longer than 310 nm and the nonnegligible uncertainty in measurements by spaceborne instruments, there is usually limited information about the vertical distribution contained in these measurements, precluding detailed profile retrievals. Consequently, it becomes necessary to place constraints on the absorber profiles, as is done in most inverse remote sensing algorithms [Rodgers, 2000]. In our algorithm, these constraints are the a priori ozone and the prescribed SO₂ profiles used to specify the relationships between the column amounts and the profiles. Doing so makes it possible to express the TOA radiances as a function of total absorber amounts as written in (1), in which their profiles have become part of the model parameters that are not the subject of retrieval. These and other model parameters, not explicitly expressed in (1), are needed as inputs for TOA radiance calculations and described in next section. In writing (1), we have also made the assumption that a scalar quantity R , which may be dependent on wavelength, can be used to describe reflections from various surfaces (i.e., Lambertian surface approximation).

[12] With these simplifications, the retrieval of the geophysical parameters: Ω , Ξ , and R can be achieved by adjusting them until TOA radiances from the forward model match the measurements at the selected wavelength bands. Given the presence of measurement and model errors, the solution to this retrieval can be expressed mathematically as the minimization of the sum of the squares of the residuals over the selected bands. Residuals are defined as the differences between the measured N values and those calculated using the forward model.

[13] The minimization problem can be further simplified by the linearization of (1). To accomplish this, a reference point, denoted by the initial state vector $\{\Omega_0, \Xi_0, R_0, c_1 = 0,$

$c_2 = 0\}$, is chosen to be the initial solution to the retrieval. Equation (1) can then be written as

$$\begin{aligned} N_m - N_0 &= \Delta\Omega \left. \frac{\partial N}{\partial \Omega} \right|_{\Omega=\Omega_0} + \Delta\Xi \left. \frac{\partial N}{\partial \Xi} \right|_{\Xi=\Xi_0} \\ &+ \left(\Delta R + \sum_{i=1}^n c_i (\lambda - \lambda_0)^i \right) \left. \frac{\partial N}{\partial R} \right|_{R=R_0} + \varepsilon_T, \end{aligned} \quad (2)$$

where $N_0 = N(\Omega_0, \Xi_0, R_0)$, $\Delta\Omega = \Omega - \Omega_0$, $\Delta\Xi = \Xi - \Xi_0$, and $\Delta R = R - R_0$. Higher-order terms are absorbed into ε_T in (2). Here R_0 is treated as independent of wavelength, and a low-order polynomial (quadratic in our current implementation, i.e., $n = 2$, c_1 and c_2 are the coefficients) is used to account for the wavelength dependence of surface reflectivity. The minimization can now be solved as the linear least square fitting of the residuals ($N_m - N_0$) for a set of measurements at different wavelength bands by the weighting functions: $\frac{\partial N}{\partial \Omega}$, $\frac{\partial N}{\partial \Xi}$, and a $\frac{\partial N}{\partial R}$ modulated polynomial of wavelength λ , with λ_0 being the reference wavelength, usually chosen to be the wavelength where R_0 is derived.

2.2. Discrete Bands

[14] The retrieval algorithm described above can make use of all the hyperspectral measurements in a wavelength window, or it can select just a few discrete wavelength bands. The main advantage of the large number of measurements over a small subset is that impacts from both systematic and random errors in the measurements can be reduced, thereby improving the quality of the retrieval results. For instance, the instrumental spectral response function and wavelength registration can be improved for hyperspectral measurements by the fitting with an extraterrestrial reference spectrum [e.g., Chance, 1998; Liu et al., 2005]. We have demonstrated that retrieval using hyperspectral GOME measurements yields more precise total ozone than using the TOMS-like discrete bands from the same measurements [Yang et al., 2004]. However, in this study, we focus on the use of the bands selected for the OMI total ozone algorithm (referred to as OMTO3) for OMI SO₂ retrieval. These OMTO3 bands, including six that center at the Earth-Probe TOMS wavelengths [McPeters et al., 1998], four that are selected for the BRD algorithm [Krotkov et al., 2006], and two additional bands in the nonabsorbed spectral region, are routinely soft calibrated [Taylor et al., 2004] to improve the quality of OMTO3 results. This set of bands samples the various parts of the SO₂ and ozone absorption spectra (see Figure 1), including both strong and weak absorbing regions. Measurements at this set of bands are adequate for SO₂ and ozone retrievals, but they are not expected to realize the full potential of the complete spectra from OMI measurements.

2.3. Forward Model

[15] The OMTO3 forward model [Dave, 1964; Bhartia and Wellemeyer, 2002; Caudill et al., 1997], named TOMRAD, is adopted to calculate the TOA radiances at the wavelength bands and the corresponding weighting functions. This vector radiative transfer model accounts for elastic molecular scattering and gaseous absorptions through the inclusion of all orders of scattering [Dave, 1964] and a pseudo-spherical correction [Caudill et al.,

1997] for more realistic handling of BU_V radiances for off-nadir viewing directions and large solar zenith angles (SZA; up to 88°).

[16] A simplifying assumption is made about surfaces, which are considered opaque and are characterized by a Lambert-equivalent reflectivity (LER), sometimes referred to as effective reflectivity. Furthermore, this LER concept is combined with an independent pixel approximation, referred to as the mixed LER (MLER) approach [Ahmad *et al.*, 2004], to account for the effects of thin or broken clouds, as is commonly done in trace gas retrievals. In the MLER approach, the TOA radiance of a partly cloudy pixel is assumed to be the weighted sum of radiances contributed from the clear and cloudy independent subpixels with fixed reflectivity (usually 0.15 and 0.8). The effective cloud pressures needed by the MLER model are taken from a satellite infrared (IR)-derived climatology data set [Bhartia and Wellemeyer, 2002; Wellemeyer *et al.*, 2004]. Aerosols are not explicitly treated in TOMRAD, but their effects on TOA radiances are partially (except for possible aerosol absorption) accounted for by adjusting and treating the effective reflectivity as a function of wavelength using a second-order polynomial.

[17] In this forward model, the ozone profile is uniquely determined by a specified column amount given the day of year and the location using the TOMS-V8 ozone profile climatology, which consists of a priori profiles for each month varying with latitude and ozone column [Bhartia and Wellemeyer, 2002; Wellemeyer *et al.*, 1997, 2004; McPeters *et al.*, 2007]. The TOMS-V8 temperature climatology is also needed to generate time- and latitudinal-dependent vertical temperature profiles, since the ozone [Daumont *et al.*, 1992; Brion *et al.*, 1993; Malicet *et al.*, 1995] and the SO₂ [Bogumil *et al.*, 2003] absorption cross sections used in the model are temperature dependent. The use of ozone and temperature climatology improves the calculations of TOA radiances by taking into account their seasonal and latitudinal variations.

[18] In the UV spectral region, rotational Raman scattering (RRS) [Joiner *et al.*, 1995; Chance and Spurr, 1997; Vountas *et al.*, 1998], which is inelastic and accounts for approximately 4% of total molecular scattering, changes the wavelength of the scattered radiation, leading to the smoothing of its prominent spectral features, such as solar Fraunhofer lines (Ring effect) and atmospheric absorption bands (telluric effect). These RRS effects can have a significant impact on the trace gas retrieval [e.g., Vountas *et al.*, 1998; Coldewey-Egbers *et al.*, 2005] if they are not properly accounted for. In our forward model, the RRS effects are included by correcting the TOMRAD radiances with filling-in factors calculated using the scalar LIDORT-RRS radiative transfer program [Spurr, 2003]. The filling-in factors, defined as the ratio of the radiance component due to inelastic scattering to that of the elastic scattering, are computed under the same atmospheric, surface, and geometrical conditions as those used in TOMRAD, insuring that the dependence of RRS effects on absorber loading, surface reflection, and viewing and illumination geometry are properly included. Note that since RRS is weakly polarizing, the filling-in factors can be accurately computed without including radiation polarization, as demonstrated by Landgraf *et al.* [2004].

[19] Current knowledge of the typical vertical SO₂ distributions for both anthropogenic and natural sources is very limited. The SO₂ from industrial air pollution as well as oxidation of natural material is likely to be confined to the planetary boundary layer (PBL), while SO₂ from effusive eruptions or degassing of volcanoes is likely to spread within a narrow layer at a height similar to the altitude of the sources, and SO₂ from explosive volcanic eruptions can be injected into the upper troposphere or lower stratosphere. Corresponding to these three scenarios, three a priori SO₂ profiles, with vertical distribution similar to the standard ozone profiles [Bhartia and Wellemeyer, 2002] in Umkehr layers 0, 1, and 3 respectively, are used in the forward model and weighting function calculations. These a priori SO₂ profiles are referred to as prescribed profiles to indicate that they are choices of convenience, and not results based on prior knowledge. An Umkehr layer is defined between two atmospheric pressure levels, $P_{atm}/2^i$ and $P_{atm}/2^{i+1}$, where i is the Umkehr layer number starting from zero and P_{atm} is equal to standard atmospheric pressure (=1013.25 hPa). The altitudes for the base of the first five Umkehr levels are roughly 0.0, 5.5, 10.3, 14.7, and 19.1 km (their precise values depend on the actual atmospheric temperature profile). The retrievals associated with the prescribed SO₂ profiles in Umkehr layers 1 and 3 are referred to as 5 KM and 15 KM retrievals respectively.

[20] The TOA radiances that are computed at a spectral resolution much higher than the OMI spectral resolution of about 0.4 nm, are then convolved with the OMI instrument spectral response function [Dobber *et al.*, 2006] to model the instrument measurements. The atmospheric weighting functions, $\frac{\partial N}{\partial \Omega}$ and $\frac{\partial N}{\partial \Xi}$, are calculated using a finite difference approach. Specifically an atmospheric weighting function is computed as the N value difference between two corresponding a priori profiles that differ by 1 Dobson Unit (DU; 1 DU = 2.69×10^{16} molecules/cm²) in total vertical column. The surface reflectivity weighting function, $\frac{\partial N}{\partial R}$, is calculated as $\frac{-100}{\ln 10} \frac{\partial I / \partial R}{I}$, where the partial derivative $\frac{\partial I}{\partial R}$ is computed analytically.

2.4. Linearization Point

[21] In principle, an arbitrary initial guess of the reference state vector can be chosen to start the retrieval process; the final state vector can be obtained by iteration until a convergence criterion is reached. However if the initial guess is too far from the correct solution, the iteration may not converge and no solution is obtained. Therefore it is desirable to choose an initial state close to the true state, so that a final state can be achieved with a minimal number of iterations.

[22] Over most of the globe, SO₂ loading is usually close to zero. So it is reasonable to set $\Xi_0 = 0$ DU, and use the operational OMTO3 algorithm to derive total ozone (Ω_0) and the wavelength-independent LER (R_0) as the initial state for the retrieval. The OMTO3 algorithm accomplishes this by matching the calculated radiances to the measured radiances at a pair of wavelengths (317.5 and 331.2 nm under most conditions, and 331.2 and 360 nm for high ozone and high SZA conditions). Starting with an initial guess of total ozone amount, the longer of the two wavelengths is used to estimate the effective surface reflectivity (or radiative cloud fraction), which is assumed to be the

same at the shorter wavelength. Next the shorter wavelength, which is highly sensitive to ozone and SO₂ absorption, is used to derive total ozone only. This process is repeated until the derived reflectivity and ozone reach their converged values. Finally this algorithm uses measurements at additional wavelengths for quality control and refinement of its retrieval results in more restricted geophysical situations. For instance, OMTO3 ozone is corrected for wavelength-dependent reflectivity errors in case of aerosol and glint using 360 nm residuals, or it is corrected for ozone profile shape errors at large SZA using 312.5 nm residuals. However, the OMTO3 algorithm does not attempt any correction for absorption by additional trace gases; only heavy SO₂ contamination is flagged by examining the residuals at multiple wavelengths [Bhartia and Wellemeyer, 2002].

2.5. Empirical Residual Correction

[23] In the presence of SO₂, the residuals calculated using (2) contain wavelength-dependent structure that correlates with the differential SO₂ absorption cross sections [Bhartia and Wellemeyer, 2002]. The residuals also have contributions from other error sources, each of which has its own spectral pattern that is superimposed on the SO₂ structure, interfering with the SO₂ retrievals. To reduce this interference, we find it necessary to perform empirical corrections to the residuals before retrieval of the final state is attempted.

[24] Various methods are used for empirical correction of SO₂ retrievals depending on the algorithm. For instance, traditional DOAS algorithm uses the reference sector approach [Khokhar et al., 2005; Richter et al., 2006]. In the BRD algorithm, the OMTO3 residuals are corrected by subtracting its corresponding orbital equatorial averages, calculated after excluding heavily SO₂ contaminated pixels [Krotkov et al., 2006]. However, forward modeling errors and instrument calibration errors are not randomly distributed over the globe. Model errors usually correlate with viewing and illumination geometry, cloud patterns, and ozone loading and its profile shape, while measurement errors, such as stray light contaminations, are affected by the scenes being observed. Taking these into consideration, we implement a new scheme, named the sliding median method, for residual correction.

[25] In this correction method, a median residual for a band is calculated for each cross-track position from a sliding group of pixels along the orbit track. This sliding group of pixels, centered on the pixel selected for correction, covers about 30° of latitude in the middle of the sunlit portion of the orbit, but the spatial extent is reduced when the selected pixel is near the terminator to ensure that a roughly equal number of pixels on either side of the selected pixel are included in the sliding group. Bad pixels identified in the linearization step and SO₂-contaminated pixels, determined by residuals that are consistent with real SO₂ and with slant column SO₂ greater than 2 DU (estimated using the BRD method [Krotkov et al., 2006]), are excluded from the sliding group. All band residuals of a pixel are corrected by subtracting the corresponding median residuals,

$$\psi^i = N_m^i - N_0^i - \langle \psi^i \rangle \quad (3)$$

where $\langle \psi^i \rangle$ is the sliding median residual of the i th wavelength band for the pixel.

[26] The 30° span of latitude is large enough to encompass sufficient background (minimal SO₂ loading) pixels, and at the same time it is small enough that the errors (of both measurement and modeling) do not change significantly within the region. This correction approach essentially forces the local median residuals of the background pixels to equal zero for all the bands. Doing so, the cross-track and latitudinal biases are reduced.

2.6. Linear Fit Algorithm

[27] Given the corrected residual ψ^i for the i th band, (2) can be rewritten as

$$\psi^i = \sum_{j=1}^5 K_{ij} x_j + \varepsilon^i \quad (4)$$

where ε^i is the remaining error for the i th band after empirical correction, and x_j is the j th component of the column vector $\mathbf{x} = \{\Delta\Omega, \Delta\Xi, \Delta R, c_1, c_2\}$, and K_{ij} is an element of the weighting function matrix (\mathbf{K} matrix [Rodgers, 2000]), i.e., the j th component of its i th row vector, $\{\frac{\partial N^i}{\partial \Omega}, \frac{\partial N^i}{\partial \Xi}, \frac{\partial N^i}{\partial R}, (\lambda_i - \lambda_0) \frac{\partial N^i}{\partial R}, (\lambda_i - \lambda_0)^2 \frac{\partial N^i}{\partial R}\}$. The least-square (LS) solution to the set of equations can be written as

$$\begin{aligned} \mathbf{x} &= (\mathbf{K}^T \cdot \mathbf{K})^{-1} \cdot \mathbf{K}^T \cdot \boldsymbol{\psi} \\ &= \mathbf{G} \cdot \boldsymbol{\psi}, \end{aligned} \quad (5)$$

where \mathbf{K}^T is the transpose matrix of \mathbf{K} , which is evaluated at the reference state. \mathbf{G} is the gain matrix, defined as $(\mathbf{K}^T \cdot \mathbf{K})^{-1} \cdot \mathbf{K}^T$, and $\boldsymbol{\psi}$ is the sliding median corrected residual column vector for all the bands. Note that the LS solution (5) assumes equal treatment (weight) for all the band residuals.

[28] Figure 2 shows a typical sample of the \mathbf{K} matrix elements, i.e., the weighting functions, which exhibit significant distinct spectral structures. These distinct behaviors in turn facilitate a stable solution to (5), meaning that small errors in measurement and forward modeling do not result in large changes in retrieved values.

[29] Figure 2 also shows that at short wavelengths (<320 nm) the measurement sensitivity to SO₂ change decreases as the SO₂ loading increases, i.e., the weighting function $\frac{\partial N^i}{\partial \Xi}$ becomes smaller with increased SO₂ amount. To account for this effect, an iterative procedure is required (especially when SO₂ loading is large), with residuals and weighting functions recalculated at each iteration step. The iterative process requires forward modeling for all the bands with various ozone and SO₂ loadings at each of steps. Usually these forward radiative transfer calculations are the most computationally intensive part of the retrieval process. To simplify the computation and improve the speed of SO₂ retrieval, we introduce the LF algorithm for further approximation by avoiding the iterative process.

[30] The LF algorithm performs its retrieval by selecting those bands whose residuals still respond nearly linearly to the change in SO₂ at the initial state (consisting of the OMTO3 total ozone, effective surface reflectivity, and zero SO₂ loading). As Figure 2 shows, the weighting functions $\frac{\partial N^i}{\partial \Xi}$ converge for the various SO₂ amounts at longer wave-

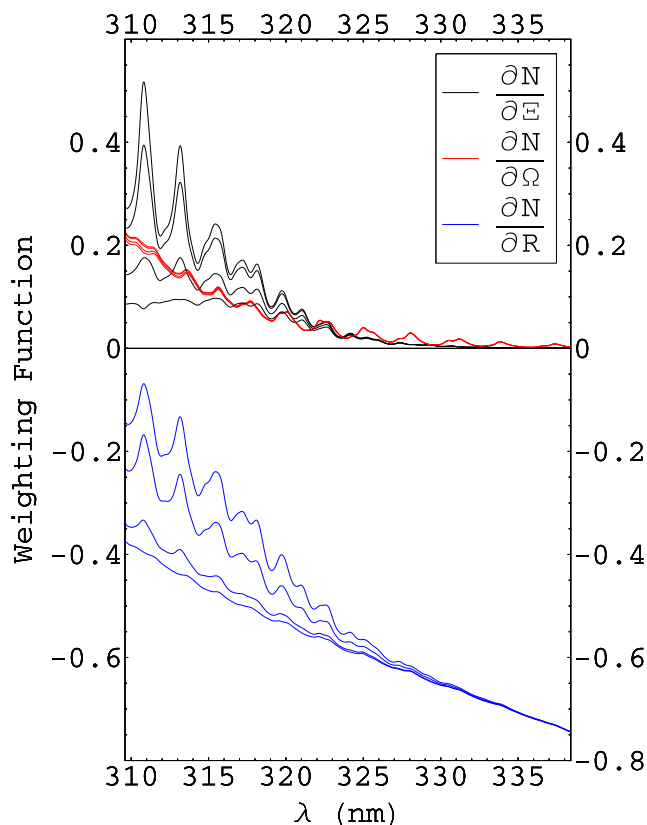


Figure 2. Weighting functions calculated for four vertical columns of SO₂: 0, 10, 50, and 100 DU (in Umkehr layer 1). Different weighting functions are represented by different colors. The black curves are $\frac{\partial N}{\partial E}$, with the units of N value per DU of SO₂ increment. The red curves are $\frac{\partial N}{\partial \Omega}$, with units of N value per DU of O₃ increment from 275 DU. The blue curves are $\frac{\partial N}{\partial R}$, with units of N value for an increase of 0.01 in reflectivity. Corresponding to increasing SO₂ amount from 0 to 100 DU, the order of the curves are from top to bottom for $\frac{\partial N}{\partial E}$ and $\frac{\partial N}{\partial \Omega}$, while the order is reversed for the curves for $\frac{\partial N}{\partial R}$.

lengths (>320 nm). In other words, measurements at longer wavelengths exhibit a more linear response to SO₂ changes. Taking advantage of this behavior, the retrieval is accomplished by solving (5) with the exclusion of residuals in wavelength bands strongly affected by nonlinear SO₂ absorption effects. As will be shown in the error analysis section later in this paper, this nonlinear absorption effect causes the LF algorithm to underestimate the SO₂ amount. Therefore in practice, this algorithm, implemented for operational SO₂ retrieval from OMI, picks as the retrieval result the largest SO₂ value derived from the process (started only when SO₂ from full band retrieval exceeds 10 DU) of dropping the shortest wavelength bands one at a time from (5) until the band centered at 322.42 nm is reached. As a result the high SO₂ retrievals from the LF algorithm are nearly always obtained with the set of measurements that start at this wavelength band.

2.7. Internal Consistency

[31] We have used the LF algorithm to process OMI measurements since its launch in July 2004, and have

produced a publicly released OMI SO₂ (called OMSO₂) data set. This data set contains numerous measurements of volcanic SO₂ emissions, ranging from low-level degassing to medium level eruptions. While in general it is very difficult to validate the SO₂ column amount retrieved from satellite measurements of a volcanic plume, mainly because of the lack of independent measurements that are comparable to the satellite observations, we nevertheless can examine the internal consistency of the retrieved geophysical parameters as an indirect way to check the validity of our results.

[32] One consistency check is to look at ozone values inside and outside of a volcanic SO₂ plume. Because of its emission from point-like sources and the subsequent dispersion and conversion into sulfate aerosols, volcanic SO₂ in the atmosphere is in general highly variable in its spatial distribution, containing a higher loading at the center of a fresh volcanic plume, but dropping off quickly toward its edges. In contrast, the actual ozone spatial distribution should behave quite smoothly; total column ozone amounts should remain almost the same inside and outside of the plume. This is particularly true in the tropics, where ozone usually exhibits a lower spatial variability compared to other locations on Earth.

[33] In the LF algorithm, the initial state is derived using the OMT03 algorithm with the assumption of zero SO₂. In the presence of SO₂, this initial ozone will be higher than its actual amount. The presence of a larger SO₂ loading will yield a larger error in initial guess, simply because the two wavelength OMT03 algorithm does not attempt to distinguish the effects of more than one absorber, and accounts for them with ozone absorption only. Consequently, the initial guess ozone distribution should show elevated values where significant SO₂ loadings are located. However, if the LF algorithm works correctly, the corrected ozone retrieved along with the SO₂ should show consistency inside and outside the volcanic plumes. To demonstrate this we show two examples of LF retrieval over volcanic plumes in Figures 3 and 4.

[34] In Figures 3 and 4, the retrieved SO₂ field is shown in Figures 3a and 4a, the LF-derived reflectivity at 331 nm is in Figures 3b and 4b, the initial ozone from OMT03 is in Figures 3c and 4c, and the corrected ozone from the LF algorithm is shown in Figures 3d and 4d. In Figure 3, the maps are the 15 KM LF results on 21 May 2006, capturing the volcanic cloud from the eruption of Soufriere Hills (Montserrat) volcano on the previous day. The plume from this eruption was injected into the stratosphere, reaching an altitude of about 18 km [Carn *et al.*, 2007a], similar to the SO₂ profile assumption made in the 15 KM LF retrieval. In Figure 4, the 5 KM LF results are shown from OMI observations on 28 November 2006 of the volcanic cloud from Nyamulagira (DR Congo).

[35] Both Figures 3c and 4c are the maps for the initial guess ozone for the LF algorithm, showing large elevated ozone values where SO₂ loadings are high. Displaying the maps of LF ozone, Figures 3d and 4d clearly demonstrate the success of this algorithm, in that the elevated initial ozone values are greatly reduced (with corrections over 100 DU for some pixels), yielding retrieved ozone values inside the volcanic plumes almost indistinguishable from those outside the plumes.

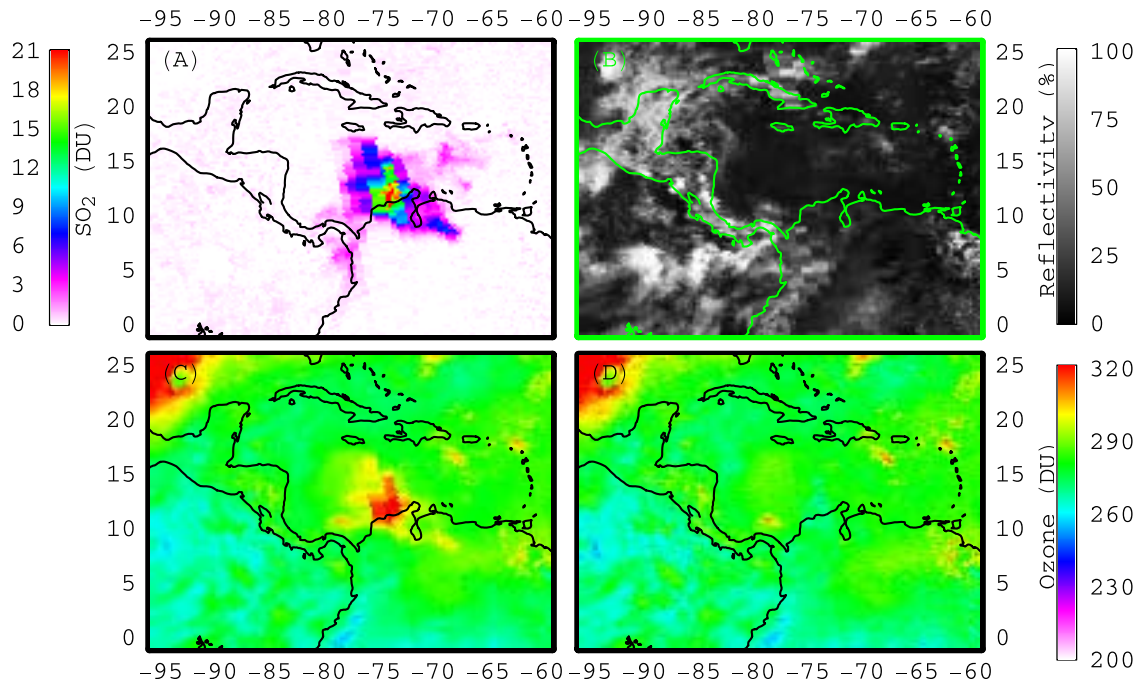


Figure 3. OMI observations (15 KM retrieval) of the volcanic plume emitted from Soufriere Hills Volcano (Montserrat; 16.72°N, 62.18°W) on 21 May 2006, following a lava dome collapse on the previous day, releasing SO₂ that reaches an altitude of 18 km [Carn *et al.*, 2007a]. (a) SO₂ column totals, (b) effective reflectivity from LF retrieval, (c) OMTO3 total ozone showing errors over the SO₂ cloud, and (d) LF corrected total ozone without errors due to SO₂. The maximum SO₂ pixel value in Figure 3a is 32.71 DU at -74.40° longitude and 11.42° latitude. The total SO₂ mass in the area shown in Figure 3a is 161 kilotons.

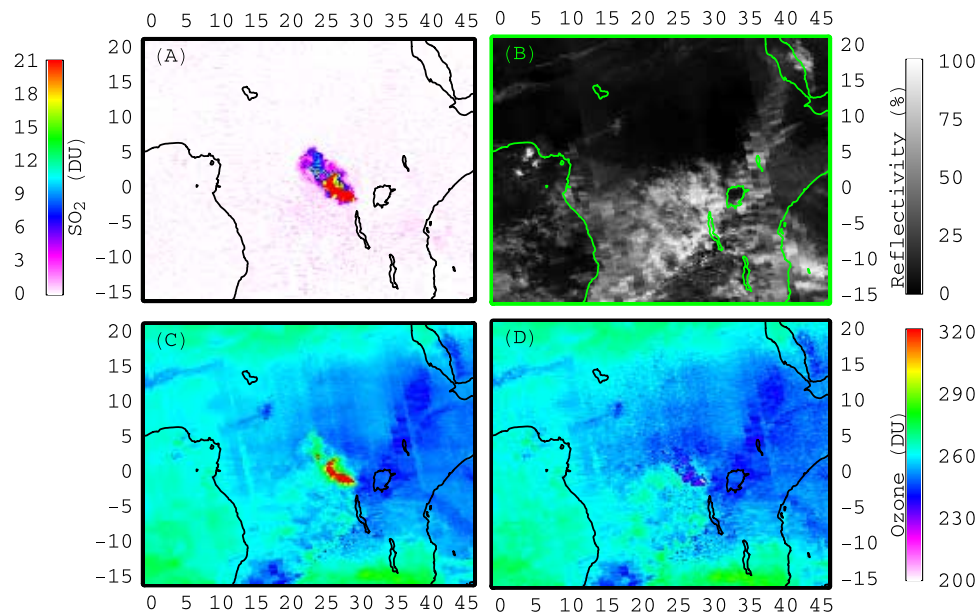


Figure 4. OMI observations (5 KM retrievals) of the volcanic plume from Nyamulagira (DR Congo; 1.41°S, 29.2°E) emitted on 28 November 2006. This volcano, which has a summit elevation about 3 km, erupted on the previous day and we assume its SO₂ plume is distributed between 3 and 10 km. The maximum SO₂ pixel value in Figure 4a is 167.65 DU at 28.46° longitude and -1.03° latitude. The total SO₂ mass in the area shown in Figure 4a is 188 kilotons. See Figure 3 caption for panel definitions.

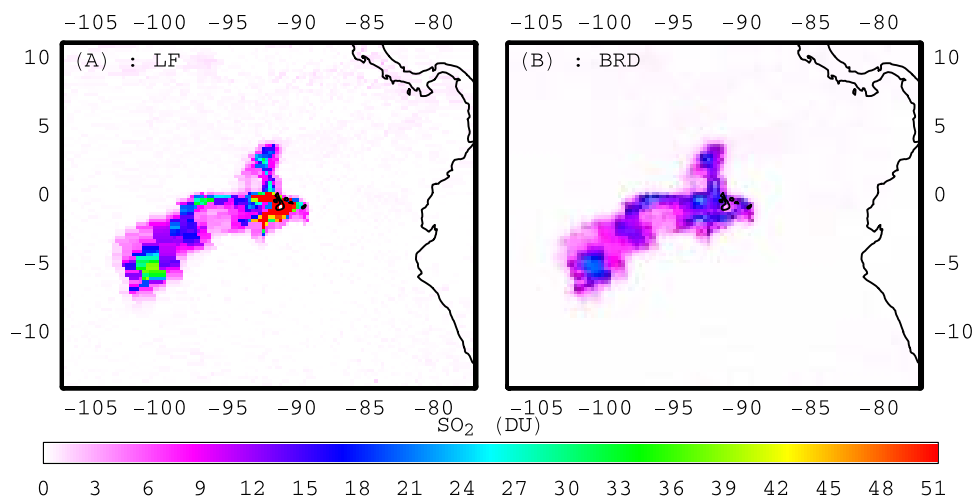


Figure 5. OMI observations of the SO₂ plume emitted from Sierra Negra volcano (summit elevation of 1124 m) in the Galapagos Islands on 23 October 2005. (a) 5 KM retrievals from LF algorithm. (b) 5 KM retrievals from BRD algorithm. The maximum SO₂ pixel value in Figure 5a is 128.26 DU at -90.88° longitude and -0.37° latitude, while the corresponding BRD SO₂ value is 6.4 DU. The total SO₂ mass in the area shown in Figure 5a is 344 kilotons, while the total mass shown in Figure 5b is 212 kilotons, i.e., BRD algorithm yields 38% less in total mass than LF retrieval for this case.

2.8. Comparison: LF Versus BRD

[36] Both the LF and BRD algorithms use the empirically corrected OMTO3 residuals as input to derive atmospheric SO₂ column amount. Though the LF algorithm may select a different subset of residuals, both share the same basic idea that these residuals contain information on atmospheric SO₂ absorption that can be converted into vertical columns. The BRD algorithm assumes that SO₂ columns are proportional to the magnitudes of differential absorptions as measured by the residual differences between the close bands, while the LF algorithm uses individual residuals in a larger subset and strives to account for other factors (including ozone and reflectivity) that affect the retrieval of SO₂ columns. It is useful to compare results for the same event from these two algorithms, so their performance and limitation can be explored.

[37] OMI SO₂ maps made from LF and BRD (5 KM) retrievals of the Sierra Negra (Galapagos Islands) volcanic plume on 23 October 2005 are displayed in Figure 5, showing the same spatial extent for both results but very different dynamic ranges in column amount distributions. The LF retrieval (Figure 5a) contains much higher SO₂ concentrations in the area immediately adjacent to the volcanic vent (located at 0.83°N , -91.17°W), and the concentrations drop off quickly as this plume is dispersing and being advected southwest. The overall BRD map (see Figure 5b) is quite similar to that of the LF, particularly in the area with low LF SO₂ concentrations, but the conspicuous difference is the complete lack of high SO₂ concentrations in the BRD map.

[38] To quantify the similarity and the difference, we show in Figure 6 all the values (within the geographic area shown in Figure 5) of ozone corrections ($\Delta\Omega$) and BRD SO₂ columns (Ξ_B) plotted against the LF SO₂ columns (Ξ_L). As we have discussed earlier in this paper, the OMTO3 total ozone algorithm accounts for all the absorbers (ozone and SO₂) by ozone absorption only. Consequently OMTO3

yields SO₂-enhanced ozone values in the volcanic plume; the larger the SO₂ loading, the higher the enhancement, therefore the greater the ozone correction by LF algorithm if it works correctly. The results in Figure 6a clearly illustrates this relationship, demonstrated the validity of LF SO₂ and ozone results.

[39] It is expected that the BRD retrieval would yield reasonable results under low SO₂ conditions, and indeed Figure 6b shows that BRD results are in good agreement with the LF results for SO₂ amounts <10 DU. Linear regression, plotted as the straight line in Figure 6b, shows that BRD SO₂ values are about 6% percent higher than the LF values. This is due to the BRD assumption of a lower and narrower vertical SO₂ profile than the prescribed profile used in the LF algorithm.

[40] However, the BRD retrieval underestimates SO₂ amounts in the presence of large SO₂ loadings, as shown in Figure 6c. The underestimation is mainly due to the nonlinear absorption effect associated with the use of a fixed set of wavelength bands in the 310.8–314.4 nm range, where both SO₂ and ozone have large absorption cross sections (see Figure 1). Starting from zero, an increase of SO₂ amount in the atmosphere manifests itself as a proportional increase in the band residual differences. As the SO₂ amount increases beyond this initial range, the nonlinear absorption effect becomes important, noticeably reducing the growth rate of band residual differences, leading to an underestimate of SO₂ amounts by the BRD algorithm, as illustrated in Figure 6c in the Ξ_L range roughly between 20 and 50 DU. As the SO₂ amount increases even further, the band residual differences reach their peak and begin to decrease; the consequence of this nonlinear effect is illustrated in Figure 6c in which the BRD values fail to increase beyond 25 DU and severe underestimation follows further SO₂ increments. In the extreme case, the SO₂ amount is so large that no band residual differences due to SO₂ are observed, and the BRD would yield an erroneous SO₂

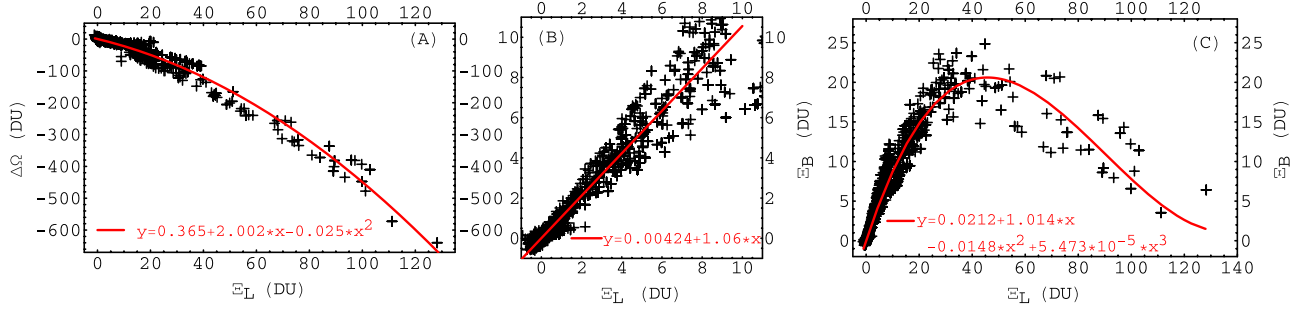


Figure 6. Data points gathered on 23 October 2005 from the geographic area shown in Figure 5 for the eruption cloud from Sierra Negra. (a) Corrections to the OMTO3 total ozone retrievals plotted against the LF column SO₂ values. (b) Comparison of BRD and LF 5 KM retrievals for total SO₂ amounts less than 10 DU in the dilute region of the plume. (c) BRD SO₂ retrievals in the entire volcanic plume compared with LF 5 KM values.

value that is completely independent of the actual SO₂ amount.

[41] Besides increasing the impact of the nonlinear effect, the presence of high SO₂ loading causes an OMTO3 ozone error, which leads to significant OMTO3 residuals at the BRD wavelength bands. The corresponding band residual differences are not equal to zero because of the nonnegligible differential ozone absorption structures at these bands. This results in an additional BRD SO₂ error that is proportional to the ozone error induced band residual differences.

[42] The LF algorithm shifts to a set of longer wavelength bands for SO₂ retrieval when the SO₂ amount increases beyond a certain threshold, and it performs simultaneous retrievals of ozone and effective reflectivity along with SO₂. The first approach reduces the impact of the nonlinear absorption effect and the second approach reduces the SO₂ error associated with the ozone error, therefore both approaches extend the valid range of LF retrievals.

3. Error Analysis

3.1. Error Expression

[43] Various error sources, from both model calculations and instrument measurements, contribute to the accuracy of the SO₂ column amount retrieved using the LF algorithm. The TOA N value function in (1), for a wavelength band i , is rewritten explicitly with all the dependent parameters and the possible errors, and is expanded with respect to the linearization point,

$$\begin{aligned} N_m^i &= N^i(\omega, \xi, R^i, \hat{b}) + \varepsilon_T^i \\ &= N^i(\omega_0, \xi_0, R_0, \hat{b}_0) + \mathbf{k}_\xi^i \cdot \Delta\xi + \mathbf{k}_\omega^i \cdot \Delta\omega \\ &\quad + k_R^i \cdot \Delta R^i + k_b^i \cdot \Delta\hat{b} + \Delta N^i + HT^i + \varepsilon_m^i. \end{aligned} \quad (6)$$

where the vector quantities, ω and ξ , are the true vertical profiles for ozone and SO₂, while ω_0 and ξ_0 , are the a priori ozone profile and the prescribed SO₂ profile, and the differences between the true and assumed profiles are $\Delta\omega = \omega - \omega_0$ and $\Delta\xi = \xi - \xi_0$. In the forward model, the atmosphere is divided into layers, and the absorber profiles are specified by their vertical layer amounts. The layer sensitivities for SO₂ and ozone are respectively defined as

$\mathbf{K}_\xi^i = \frac{\partial N^i}{\partial \xi} |_{\xi=\xi_0}$ and $\mathbf{K}_\omega^i = \frac{\partial N^i}{\partial \omega} |_{\omega=\omega_0}$. R^i is the true reflectivity of the wavelength band and this expression of reflectivity is more general than the polynomial characterization of its dependence on wavelength used in (2). The reflectivity sensitivity is $k_R^i = \frac{\partial N^i}{\partial R} |_{R=R_0}$ and the difference is $\Delta R = R^i - R_0$. Respectively, \hat{b} and \hat{b}_0 refer to the true model parameter values and those used in the linearization, the parameter error is $\Delta\hat{b} = \hat{b} - \hat{b}_0$, and the corresponding parameter sensitivity is $k_b^i = \frac{\partial N^i}{\partial \hat{b}} |_{\hat{b}=\hat{b}_0}$. These parameters include the atmospheric temperature profiles, the angles that specify illumination and viewing geometry, and the effective cloud pressure, the spectroscopic constants of ozone and SO₂, and the parameters that determine the spectral response function of the instrument. ΔN^i are the forward model errors such as incomplete accounting for RRS effects and other possible imperfections in the radiative transfer calculations. HT^i refers to the higher-order terms that are truncated in the LF algorithm. The last term ε_m^i is the total measurement error of the instrument, including the errors in radiometric and wavelength calibration, and the random measurement noise.

[44] Using the definitions of the column vector \mathbf{x} and the sliding-median corrected residual ψ , we can rewrite (5) as

$$\begin{aligned} \mathbf{V}_L - \mathbf{V}_0 &= \mathbf{G} \cdot \psi \\ &= \mathbf{G} \cdot (\mathbf{N}_m - \mathbf{N}(\omega_0, \xi_0, R_0, \hat{b}_0) - \langle \psi \rangle), \end{aligned} \quad (7)$$

where $\mathbf{V}_0 = \{\Omega_0, \Xi_0 = 0, R_0, 0, 0\}$ is the column vector of the initial guess derived using the OMTO3 total ozone algorithm, while $\mathbf{V}_L = \{\Omega_L, \Xi_L, R_L, c_1, c_2\}$ is the column vector derived using the LF algorithm.

[45] To see how the model and measurement errors propagate into the final results, substituting \mathbf{N}_m in (7) with (6), (7) can be rewritten as

$$\begin{aligned} \mathbf{V}_L - \mathbf{V}_0 &= \mathbf{G} \cdot (\mathbf{k}_\xi \cdot \Delta\xi + \mathbf{HT}) \\ &\quad + \mathbf{G} \cdot (\mathbf{k}_\omega \cdot \Delta\omega + \mathbf{k}_R \Delta R + \mathbf{k}_b \cdot \Delta\hat{b}) \\ &\quad + \mathbf{G} \cdot (\Delta N + \varepsilon_m - \langle \psi \rangle). \end{aligned} \quad (8)$$

We have dropped the label i from the scalar variables in (6) and expressed them as column vectors (written in bold typeface) in (8), with their column dimensions equal to the number of wavelength bands used in the LF algorithm.

Similarly, the label i for row vectors in (6) has been dropped and these row vectors have become matrices with their column dimensions equal to the number of wavelength bands.

[46] In general, the true effective reflectivity is a smooth function of wavelength in the UV range, and this function can be described accurately by a low-order polynomial. When the absorber loadings are low, \mathbf{k}_R contains a small amount of high-frequency structure (see Figure 2), though this increases in magnitude as the absorber loading increases, particularly at wavelengths where the nonlinear effect dominates. However the initial estimate of the effective reflectivity from the OMTO3 algorithm is very good because of the use of a wavelength in the weak absorption region, therefore the reflectivity error $\Delta\mathbf{R}$ is expected to be very small (at the level of 0.001). Consequently the term $\mathbf{k}_R\Delta\mathbf{R}$ varies smoothly with wavelength, acting like a high-pass filter that removes the overall bias in the residuals. The remainder of the high-frequency component in this term can be absorbed into the higher-order term \mathbf{HT} .

[47] The sliding median $\langle\psi\rangle$ subtracted from the residuals in (8) essentially cancels those terms that are smooth in their spatial variations. These spatially slow-varying terms include the ozone profile error and some of the model parameter errors such as those due to the use of a climatological temperature profile. Some forward model and systematic measurement errors, which usually do not change drastically from one spatial location to another, are also reduced to nearly zero by this correction scheme. However, highly spatially variable terms, such as those errors induced by the presence of SO₂, the random component of the measurement error and the effective cloud pressure error, are largely left intact in this scheme. The SO₂-induced errors are the profile shape error and the higher-order term, which becomes important when SO₂ loading is high. On the basis of these considerations, (8) is rewritten as follows,

$$\begin{aligned} \mathbf{V}_L - \mathbf{V}_0 &= \mathbf{G} \cdot \mathbf{k}_\xi \cdot \Delta\xi + \mathbf{G} \cdot \mathbf{HT} + \mathbf{G} \cdot \varepsilon_r \\ &= \mathbf{A} \cdot (\xi - \xi_0) + \mathbf{G} \cdot \mathbf{HT} + \mathbf{G} \cdot \varepsilon_r, \end{aligned} \quad (9)$$

where the matrix $\mathbf{A} = \mathbf{G} \cdot \mathbf{K}_\xi$ is the averaging kernel [e.g., Rodgers, 2000; Eskes and Boersma, 2003]. The remaining error after the sliding median correction is $\varepsilon_r = \mathbf{K}_\omega \cdot \Delta\omega + \mathbf{K}_R \Delta\mathbf{R} + \mathbf{k}_b \cdot \Delta b + \Delta\mathbf{N} + \varepsilon_m - \langle\psi\rangle$, and it is essentially equal to the random noise of the measurement, but may also contain errors that do not vary smoothly from one pixel to the next, such as the error caused by using the wrong effective cloud pressure when cloud is present.

[48] The row equation that refers to the SO₂ column amount can be extracted from (9), and after subtracting $\Xi_T - \Xi_0$ from both sides of this row equation it can be rewritten as

$$\Xi_L - \Xi_T = (\mathbf{A}_\Xi - \mathbf{1}) \cdot (\xi - \xi_0) + \mathbf{G}_\Xi \cdot \mathbf{HT} + \mathbf{G}_\Xi \cdot \varepsilon_r, \quad (10)$$

where Ξ_T is the true SO₂ column amount, obtained by the summation of the true SO₂ vertical profile ξ . The row vectors, \mathbf{A}_Ξ and \mathbf{G}_Ξ , are extracted from the matrices, \mathbf{A} and \mathbf{G} , the corresponding rows that are specific to the computation of SO₂ amount Ξ_L . The row vector $\mathbf{1}$ in (10) contains the value 1 for all its elements; its dot product with

a vertical profile (a column vector) yields the total column, i.e., the summation of all the individual layer amounts.

[49] The error expression (10) for SO₂ from the LF algorithm relates the vertical column derived from the LF algorithm to the true vertical column, and its first two terms on the right hand side are the direct consequences of the two assumptions made in the LF algorithm. These two assumptions are the linearization of the forward model and the use of prescribed SO₂ profiles, which determine the unique vertical distribution given the total column amounts. It is obvious that both of these assumptions could be wrong, since the actual SO₂ vertical distribution for an observation is likely to be different from the prescribed one, and nonlinear effects are expected to be significant when SO₂ loading is large, leading to errors in retrieval results.

3.2. SO₂ Profile Error

[50] Though the values of the averaging kernel as a function of atmospheric pressure level differ from one pixel to the next, depending on the actual geophysical conditions, its functional behavior or shape remains basically unchanged given the same prescribed SO₂ profile for the cloud-free pixel. For a cloudy pixel, the shape of the averaging kernel can be altered significantly compared to the cloud free pixel depending on the radiative cloud fraction and the cloud pressure. Figure 7 shows three examples of averaging kernels under typical conditions for the LF algorithm with prescribed profiles used in the operational SO₂ retrievals. On the basis of these examples, retrieval errors can be estimated quantitatively given the actual SO₂ profiles.

[51] For instance, if the actual SO₂ layer is located lower than the uniform SO₂ profile in Umkehr layer 1 (~5–10 km) used in the LF algorithm, the retrieval will underestimate the SO₂ column for a cloud-free pixel with low surface reflectivity, retrieving as low as about half of the actual column amount if the actual SO₂ is at ground level, i.e., at the bottom of Umkehr layer 0. On the other hand, if the actual SO₂ layer is higher than the prescribed SO₂ profile, e.g., in Umkehr layers 2 to 6 (i.e., between 15 and 35 km), the LF algorithm will overestimate the SO₂ column by 20% at most. However, if the SO₂ distribution goes even higher in altitude, say beyond Umkehr layer 7 (>35 km), the 5 KM retrieval will underestimate the SO₂ column slightly, usually by no more than a few percent of the actual value.

[52] The errors associated with the 15 KM LF retrieval (with prescribed SO₂ profile distributed in Umkehr layer 3) behave differently compared with the 5 KM retrieval. For a cloud-free pixel with 10% ground reflectivity, if the actual SO₂ layer is slightly below the prescribed level, i.e., in Umkehr layer 2, the 15 KM retrieval will overestimate the SO₂ column by no more than 5%. However if the actual layer is in Umkehr layers 1 or 0, the 15 KM retrieval will underestimate the actual SO₂ column, and the lower the actual layer, the larger the error, down to a retrieved column that could be slightly less than half of the actual column. If the actual SO₂ is higher than the prescribed profile, e.g., in Umkehr layer 4 or higher, the 15 KM retrieval will also underestimate the SO₂ column, usually by no more than 10% of the actual column.

[53] For a cloudy pixel, the error analysis becomes much more complicated, even in the case when the correct cloud top pressure is used in the retrieval. This is in part due to the

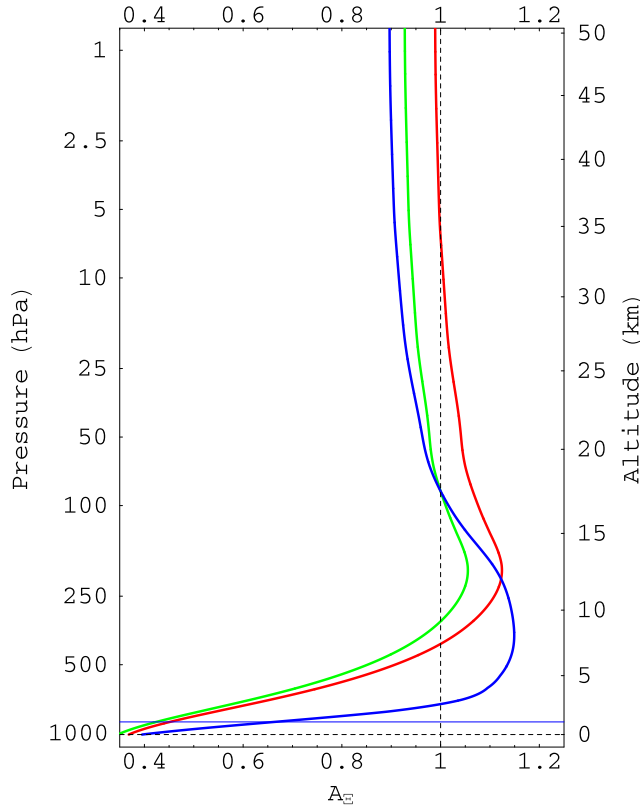


Figure 7. Examples of the averaging kernel (A_{Ξ}) for SO₂ retrievals. The red curve is for a cloud-free pixel with a surface reflectivity of 0.1 and a prescribed SO₂ profile in Umkehr layer 1. The green curve represents identical conditions to the red curve except that SO₂ is distributed in Umkehr layer 3. The blue curve is for the same SO₂ profile as the green curve in a partially cloud-covered pixel with a radiative cloud fraction of 33% and a cloud pressure of 892 hPa, indicated by the thin horizontal blue line.

fact that the MLER model used here is too simple to yield reliable quantitative estimates in the case when the absorber is below or mixing with the cloud. However the MLER model should work well enough when the absorber is above the cloud. In the example shown as the blue curve in Figure 7 for a pixel with 33% radiative cloud fraction, if the actual SO₂ is located below the prescribed profile but above the cloud, the 15 KM retrieval will overestimate the column amount by as much as 20%. However if the actual distribution is above the prescribed profile, the 15 KM retrieval will underestimate the SO₂ column, usually by no more than 15%.

3.3. Nonlinear Effect Error

[54] As shown earlier in the comparison between LF and BRD (section 2.8), the nonlinear absorption effect causes the underestimation of BRD retrievals when SO₂ columns are greater than 10 DU. In this section, we will show that this effect has a similar impact on LF retrievals, but only for much higher SO₂ column amounts.

[55] To examine the nonlinear effect error in the LF algorithm, we look at cases in which the prescribed SO₂ vertical profile is close to the actual profile. In these cases

the term \mathbf{HT} in (10) can be estimated if we use only the second-order term (i.e., third-order term and higher are truncated)

$$\mathbf{HT} = \frac{\partial^2 \mathbf{N}}{\partial \Xi^2} \Big|_{\Xi=\Xi_0} (\Xi - \Xi_0)^2. \quad (11)$$

As the SO₂ column amount increases, the weighting function $\frac{\partial \mathbf{N}}{\partial \Xi}$ becomes smaller, and this behavior is clearly illustrated in Figure 2. This implies that the second derivative, $\frac{\partial^2 \mathbf{N}}{\partial \Xi^2}$, is negative, and its absolute value gets larger with increasing SO₂ absorption. Namely the second derivative has a structure that is anticorrelative with its first derivative (i.e., the SO₂ weighting function). Therefore the higher-order term \mathbf{HT} behaves much like a negative absorber, and the second term in (10) will yield a negative SO₂ column amount. In other words, the LF retrieval underestimates a SO₂ column with the linearization of the forward model.

[56] In order to take advantage of the fast computation of the forward model and the simple implementation of algorithm steps, this technique always sets the initial guess of the SO₂ column (Ξ_0) to be zero. Consequently the term $\Xi - \Xi_0$ can be very large, particularly when the actual vertical column is high, resulting in a significant contribution from the higher-order term, which leads to the underestimation of the actual SO₂ column. The algorithm mitigates this problem by dropping the shorter wavelength bands, which are affected more by the nonlinear effect, therefore extending the valid range of LF retrievals. Using an iterative algorithm, which would eliminate the nonlinear effect error as discussed later in this paper, we have estimated the error in the LF algorithm when SO₂ loading is high, and found that the LF retrieval can underestimate the SO₂ column by as much as 70% (the precise error depends on the geophysical conditions) when the actual column is ~ 400 DU because of the linearization of the forward model at zero SO₂. However, this error is much less when the SO₂ loading is lower and it is at the 20% level when the actual column amount is around 100 DU.

3.4. Cloud Pressure Error

[57] One of the forward model parameters needed for the computation of TOA radiances and the weighting functions in the LF algorithm is the effective cloud pressure (p) associated with the MLER model. A climatological cloud pressure data set derived from IR satellite measurements is used in the currently released OMI SO₂ product. In general (but not always) the IR-derived climatological cloud pressures are lower (i.e., cloud is placed at a higher altitude) than the effective cloud pressures that are consistent with the MLER model used in this algorithm, therefore introducing additional errors for cloudy observations.

[58] To analyze the impact of cloud pressure error (Δp), (10) is rewritten explicitly with the cloud pressure,

$$\begin{aligned} \Xi_L - \Xi_T &= (\mathbf{A}_{\Xi} - \mathbf{1}) \cdot (\xi - \xi_0) + \mathbf{G}_{\Xi} \cdot \mathbf{HT} \\ &+ \mathbf{G}_{\Xi} \cdot \frac{\partial \mathbf{N}}{\partial p} \Big|_{p=p_0} \Delta p + \mathbf{G}_{\Xi} \cdot \varepsilon^*, \end{aligned} \quad (12)$$

where ε_r^* is ε_r less the cloud pressure induced error. Note that the averaging kernel \mathbf{A}_Ξ , the higher-order term \mathbf{HT} , and the gain matrix \mathbf{G}_Ξ , are all dependent on the cloud pressure. If the cloud pressure error is not too large, its impact on the retrieval can be estimated with just the third term on the right hand side of (12). The cloud pressure sensitivity $\frac{\partial N}{\partial p}$ contains high-frequency spectral structure (similar to the RRS filling structure), which has certain degree of correlation with the SO₂ absorption structure. Given that the cloud pressure errors Δp are mostly positive, the OMI SO₂ shows consistent error patterns over clouds, and these patterns contain elevated SO₂ values that are mostly less than 1.5 DU for 5 KM retrievals. Note that SO₂ emissions from degassing volcanoes are usually in the range of a few DU, this cloud-related SO₂ error may interfere with the measurements of these emissions.

[59] When the cloud pressure error is very large, the actual averaging kernel is quite different from its initial estimate, and the higher-order terms become dominant, making this analysis not applicable to these situations. Fortunately, cloud pressures consistent with the MLER model are being retrieved from OMI using approaches based on RRS [Joiner *et al.*, 2004, 2006; Vasilkov *et al.*, 2004] or absorption in the O₂ – O₂ band near 477 nm [Acarreta *et al.*, 2004]. Using OMI-derived cloud pressures will significantly reduce the cloud pressure errors, resulting in a more accurate SO₂ retrieval in our next release of the product.

4. Limitations and Improvements

[60] Both anthropogenic and volcanic emissions contribute to an enormous dynamic variation in atmospheric SO₂ concentrations not observed in any other trace gases. The vast SO₂ loading range and its uncertainty in vertical distribution, coupled with the interference from ozone absorption, poses a unique challenge for accurate SO₂ retrieval.

[61] Previously we have developed the BRD technique [Krotkov *et al.*, 2006], which maximizes the detection sensitivity to small concentrations of SO₂ in the planetary boundary layer, but nonlinear effect and ozone-error induced residuals have limited the valid range of BRD retrievals to SO₂ vertical columns of about 10 DU.

[62] The LF algorithm described in this paper has greatly extended the valid range of SO₂ retrievals by shifting the wavelength bands to the weaker absorption region and by performing simultaneous retrievals of SO₂, ozone, and effective reflectivity. However our error analysis has indicated that when SO₂ loadings are very large, the nonlinear effect can still lead to severe under estimation of the actual column amounts. This is the main factor that limits the valid range of this algorithm to about 100 DU, with an overall uncertainty of about 20%. Note that the use of longer wavelength bands makes the LF algorithm more susceptible to measurement errors and the errors in the SO₂ absorption cross sections, which are less accurate in the longer (>325 nm) wavelength region than those in the shorter (between 310 and 325 nm) wavelength region. Therefore even with the availability of hyperspectral measurements, it may not be practical to avoid dealing with the

nonlinear effect by shifting to measurements at even longer wavelengths.

[63] Fortunately we can greatly reduce the impact of this nonlinear effect on the SO₂ retrieval by iteration without limitation to the use of longer wavelength bands. All the equations presented in this paper are equally valid and can be used without any modification in the iterative retrieval, which can be implemented as the repeated application of LF algorithm steps, each of which takes the state vector derived at the previous step as its new linearization point, similar to the steps in the modified Krueger-Kerr algorithm [Krueger *et al.*, 2000]. Doing so, Ξ_0 would approach the correct value, so that the term $(\Xi - \Xi_0)^n$ (with $n = 2$ and higher) would become so small that the higher-order term becomes negligible. We are currently developing and implementing the iterative algorithm, which is expected to be valid over the complete SO₂ range.

[64] The error analysis (which would be valid for the iterative algorithm also) of the LF algorithm has found that the prescribed SO₂ profiles have significant impacts on the retrieval results depending on the difference between actual and prescribed profiles. The error in SO₂ retrieval contributed by this uncertainty in the SO₂ vertical distribution is mostly limited to less than 20% if the actual SO₂ is not located near the bottom of Umkehr layer 0. To improve the accuracy of SO₂ retrieval, it is necessary to have better information on its vertical distribution, either obtained from other sources such as the output from chemistry-transport models or derived from the same BUUV measurements. It is possible to perform limited vertical SO₂ profile retrievals from the hyperspectral OMI measurements.

5. Conclusions

[65] We have presented the LF algorithm developed for the simultaneous retrievals of vertical columns of SO₂, ozone, and effective reflectivity from the OMI BUUV measurements of OMI. The sample results have demonstrated the success of this algorithm, with which large elevated ozone values in the volcanic plumes from the total ozone algorithm are greatly reduced so that consistent ozone values are retrieved both inside and outside the plumes.

[66] We have also derived an absolute error expression for retrievals from this algorithm and used it to perform detailed analysis of the various factors that affect the retrieved SO₂ columns and provide quantitative estimates of their error contributions. The averaging kernel derived along with the error expression is very useful in understanding the altitude-dependent sensitivity of this algorithm, and provides the necessary information to interpret the retrievals. The averaging kernel is needed in comparisons between in situ profile measurements and satellite retrievals and in application of data assimilation [Rodgers, 2000].

[67] The LF algorithm is very fast when applied to measurements at a small set of discrete wavelengths and produce reasonable estimates of vertical columns for a wide range of conditions. Therefore it is able to provide data needed in aviation and ground hazard management for near real-time monitoring and tracking of volcanic clouds.

[68] The LF algorithm is also very flexible in terms of measurement input; it can be applied to the discrete bands from TOMS, or some optimally selected discrete UV

bands from the hyperspectral measurements of GOME, SCIAMACHY or OMI, or it can take advantage of their full spectral measurements in selected wavelength windows. Because of this built-in algorithm flexibility, it is an ideal choice for making a long-term consistent SO₂ data record using past (TOMS, GOME), present (OMI, SCIAMACHY, GOME-2), and future (GOME-2, OMPS (Ozone Mapping and Profiler Suite)) UV measurements from instruments on satellite platforms.

[69] **Acknowledgments.** The Dutch-Finnish built OMI instrument is part of the NASA EOS Aura satellite payload. The OMI project is managed by the Netherlands Agency for Aerospace Program (NIVR) and the Royal Dutch Meteorological Institute (KNMI). This work was supported in part by NASA under grant NNS06AA05G (NASA volcanic cloud data for aviation hazards) and by the U.S. OMI Science Team. The authors would like to thank the KNMI OMI team for producing LIB radiance data and the U.S. OMI operational team for continuing support.

References

- Acarreta, J. R., J. F. De Haan, and P. Stammes (2004), Cloud pressure retrieval using the O₂-O₂ absorption band at 477 nm, *J. Geophys. Res.*, *109*, D05204, doi:10.1029/2003JD003915.
- Ahmad, Z., P. K. Bhartia, and N. Krotkov (2004), Spectral properties of backscattered UV radiation in cloudy atmospheres, *J. Geophys. Res.*, *109*, D01201, doi:10.1029/2003JD003959.
- Bhartia, P. K., and C. W. Wellemeyer (2002), TOMS-V8 Total O₃ Algorithm, in *Algorithm Theoretical Basis Document: OMI Ozone Products, ATBD-OMI-02*, version 2.0, vol. II, edited by P. K. Bhartia, pp. 15–31, NASA Goddard Space Flight Cent., Greenbelt, Md. (Available at http://eosps0.gsfc.nasa.gov/eos_homepage/for_scientists/atbd/docs/OMI/ATBD-OMI-02.pdf)
- Bogumil, K., et al. (2003), Measurements of molecular absorption spectra with the SCIAMACHY pre-flight model: Instrument characterization and reference data for atmospheric remote-sensing in the 230–2380 nm region, *J. Photochem. Photobiol. A Chem.*, *157*, 167–184, doi:10.1016/S1010-6030(03)00062-5.
- Bovensmann, H., J. P. Burrows, M. Buchwitz, J. Frerick, S. Noël, V. V. Rozanov, K. V. Chance, and A. P. H. Goede (1999), SCIAMACHY: Mission objectives and measurement modes, *J. Atmos. Sci.*, *56*(2), 127–150, doi:10.1175/1520-0469(1999)056<0127:SMOAMM>2.0.CO;2.
- Bramstedt, K., A. Richter, M. Van Roozendaal, and I. De Smedt (2004), Comparisons of SCIAMACHY sulfur dioxide observations, in *Proceedings of the 2nd Workshop on the Atmospheric Validation of Envisat (ACVE-2)*, Eur. Space Agency Spec. Publ. [CD-ROM], ESA SP-562, 11.1–11.4.
- Brion, J., A. Chakir, D. Daumont, J. Malicet, and C. Parisse (1993), High-resolution laboratory absorption cross section of O₃. Temperature effect, *Chem. Phys. Lett.*, *213*(5–6), 512–610, doi:10.1016/0009-2614(93)89169-I.
- Buchwitz, M., V. V. Rozanov, and J. P. Burrows (2000), A near-infrared optimized DOAS method for the fast global retrieval of atmospheric CH₄, CO, CO₂, H₂O, and N₂O total column amounts from SCIAMACHY Envisat-1 nadir radiances, *J. Geophys. Res.*, *105*(D12), 15,231–15,246.
- Burrows, J. P., et al. (1999), The Global Ozone Monitoring Experiment (GOME): Mission concept and first scientific results, *J. Atmos. Sci.*, *56*, 151–175, doi:10.1175/1520-0469 [1999]056<0151:TGOMEG>2.0.CO;2.
- Cam, S. A., A. J. Krueger, G. J. S. Bluth, S. J. Schaefer, N. A. Krotkov, I. M. Watson, and S. Datta (2003), Volcanic eruption detection by the Total Ozone Mapping Spectrometer (TOMS) instruments: A 22-year record of sulphur dioxide and ash emissions, in *Volcanic Degassing*, edited by C. Oppenheimer, D. M. Pyle, and J. Barclay, *Spec. Publ. Geol. Soc. London*, *213*, 177–202.
- Carn, S. A., N. A. Krotkov, K. Yang, R. M. Hoff, A. J. Prata, A. J. Krueger, S. C. Loughlin, and P. F. Levelt (2007a), Extended observations of volcanic SO₂ and sulfate aerosol in the stratosphere, *Atmos. Chem. Phys. Disc.*, *7*, 2857–2871.
- Cam, S. A., A. J. Krueger, N. A. Krotkov, K. Yang, and P. F. Levelt (2007b), Sulfur dioxide emissions from Peruvian copper smelters detected by the Ozone Monitoring Instrument, *Geophys. Res. Lett.*, *34*, L09801, doi:10.1029/2006GL029020.
- Caudill, T. R., D. E. Flittner, B. M. Herman, O. Torres, and R. D. McPeters (1997), Evaluation of the pseudo-spherical approximation for backscattered ultraviolet radiances and ozone retrieval, *J. Geophys. Res.*, *102*(D3), 3881–3890.
- Chance, K. (1998), Analysis of BrO measurements from the Global Ozone Monitoring Experiment, *Geophys. Res. Lett.*, *25*(17), 3335–3338.
- Chance, K. V., and R. J. D. Spurr (1997), Ring effect studies: Rayleigh scattering, including molecular parameters for rotational Raman scattering, and the Fraunhofer spectrum, *Appl. Opt.*, *36*, 5224–5230.
- Coldeewey-Egbers, M., M. Weber, L. N. Lamsal, R. de Beek, M. Buchwitz, and J. P. Burrows (2005), Total ozone retrieval from GOME UV spectral data using the weighting function DOAS approach, *Atmos. Chem. Phys.*, *5*, 1015–1025.
- Daumont, D., J. Brion, J. Charbonnier, and J. Malicet (1992), Ozone UV spectroscopy. I: Absorption cross-sections at room temperature, *J. Atmos. Chem.*, *15*, 145–155, doi:10.1007/BF00053756.
- Dave, J. V. (1964), Meaning of successive iteration of the auxiliary equation of radiative transfer, *Astrophys. J.*, *140*, 1292–1303.
- Dobber, M. R., et al. (2006), Ozone Monitoring Instrument calibration, *IEEE Trans. Geosci. Remote Sens.*, *44*(5), 1209–1238, doi:10.1109/TGRS.2006.869987.
- Eisinger, M., and J. P. Burrows (1998), Tropospheric sulfur dioxide observed by the ERS-2 GOME instrument, *Geophys. Res. Lett.*, *25*, 4177–4180.
- Eskes, H. J., and K. F. Boersma (2003), Averaging kernels for DOAS total-column satellite retrievals, *Atmos. Chem. Phys.*, *3*, 1285–1291.
- Gurevich, G. S., and A. J. Krueger (1997), Optimization of TOMS wavelength channels for ozone and sulfur dioxide retrievals, *Geophys. Res. Lett.*, *24*(17), 2187–2190.
- Joiner, J., and P. K. Bhartia (1997), Accurate determination of total ozone using SBUV continuous spectral scan measurements, *J. Geophys. Res.*, *102*(D11), 12,957–12,970.
- Joiner, J., P. K. Bhartia, R. P. Cebula, E. Hilsenrath, R. D. McPeters, and H. Park (1995), Rotational Raman scattering (ring effect) in satellite backscatter ultraviolet measurements, *Appl. Opt.*, *34*, 4513–4525.
- Joiner, J., A. P. Vasilkov, D. E. Flittner, J. F. Gleason, and P. K. Bhartia (2004), Retrieval of cloud pressure and oceanic chlorophyll content using Raman scattering in GOME ultraviolet spectra, *J. Geophys. Res.*, *109*, D01109, doi:10.1029/2003JD003698.
- Joiner, J., A. P. Vasilkov, K. Yang, and P. K. Bhartia (2006), Observations over hurricanes from the ozone monitoring instrument, *Geophys. Res. Lett.*, *33*, L06807, doi:10.1029/2005GL025592.
- Khokhar, M. F., C. Frankenberg, M. Van Roozendaal, S. Beirle, S. Khl, A. Richter, U. Platt, and T. Wagner (2005), Satellite observations of atmospheric SO₂ from volcanic eruptions during the time-period of 1996–2002, *Adv. Space Res.*, *36*(5), 879–887, doi:10.1016/j.asr.2005.04.114.
- Krotkov, N. A., A. J. Krueger, and P. K. Bhartia (1997), Ultraviolet optical model of volcanic clouds for remote sensing of ash and sulfur dioxide, *J. Geophys. Res.*, *102*(D18), 21,891–21,904.
- Krotkov, N. A., O. Torres, C. Seftor, A. J. Krueger, A. Kostinski, W. I. Rose, G. J. S. Bluth, D. Schneider, and S. J. Schaefer (1999a), Comparison of TOMS and AVHRR volcanic ash retrievals from the August 1992 eruption of Mt. Spurr, *Geophys. Res. Lett.*, *26*(4), 455–458.
- Krotkov, N. A., D. E. Flittner, A. J. Krueger, A. Kostinski, C. Riley, W. Rose, and O. Torres (1999b), Effect of particle non-sphericity on satellite monitoring of drifting volcanic ash clouds, *J. Quant. Spectrosc. Radiat. Transfer*, *63*, 613–630, doi:10.1016/S0022-4073(99)00041-2.
- Krotkov, N. A., S. A. Carn, A. J. Krueger, P. K. Bhartia, and K. Yang (2006), Band residual difference algorithm for retrieval of SO₂ from the Aura Ozone Monitoring Instrument (OMI), *IEEE Trans. Geosci. Remote Sens.*, *44*(5), 1259–1266, doi:10.1109/TGRS.2005.861932.
- Krotkov, N., A. Krueger, K. Yang, S. Carn, P. K. Bhartia, and P. Levelt (2007), SO₂ Data from the Ozone Monitoring Instrument (OMI), paper presented at Envisat Symposium 2007, Eur. Space Agency, Montreux, Switzerland.
- Krueger, A. J. (1983), Sighting of El Chichon Sulfur Dioxide Clouds with the Nimbus 7 Total Ozone Mapping Spectrometer, *Science*, *220*, 1377–1379, doi:10.1126/science.220.4604.1377.
- Krueger, A. J., L. S. Walter, P. K. Bhartia, C. C. Schnetzler, N. A. Krotkov, I. Sprod, and G. J. S. Bluth (1995), Volcanic sulfur dioxide measurements from the total ozone mapping spectrometer instruments, *J. Geophys. Res.*, *100*, 14,057–14,076.
- Krueger, A. J., S. J. Schaefer, N. Krotkov, G. Bluth, and S. Barker (2000), Ultraviolet remote sensing of volcanic emissions, in *Remote Sensing of Active Volcanism*, *Geophys. Monogr. Ser.*, vol. 116, edited by P. J. Mougins-Mark, J. A. Crisp, and J. H. Fink, pp. 25–43, AGU, Washington, D. C.
- Landgraf, J., O. P. Hasekamp, R. van Deelen, and I. Aben (2004), Rotational Raman scattering of polarized light in the Earth atmosphere: A vector radiative transfer model using the radiative transfer perturbation theory approach, *J. Quant. Spectrosc. Radiat. Transfer*, *87*(3–4), 399–433, doi:10.1016/j.jqsrt.2004.03.013.

- Levelt, P. F., G. H. J. van den Oord, M. R. Dobber, A. Mälkki, H. Visser, J. de Vries, P. Stammes, J. Lundell, and H. Saari (2006), The Ozone Monitoring Instrument, *IEEE Trans. Geosci. Remote Sens.*, *44*(5), 1093–1101, doi:10.1109/TGRS.2006.872333.
- Liu, X., K. V. Chance, C. E. Sioris, R. J. D. Spurr, T. P. Kurosu, R. V. Martin, and M. J. Newchurch (2005), Ozone profile and tropospheric ozone retrievals from the Global Ozone Monitoring Experiment: Algorithm description and validation, *J. Geophys. Res.*, *110*, D20307, doi:10.1029/2005JD006240.
- Malicet, J., D. Daumont, J. Charbonnier, C. Parisse, A. Chakir, and J. Brion (1995), Ozone UV spectroscopy, II: Absorption cross-sections and temperature dependence, *J. Atmos. Chem.*, *21*, 263–273, doi:10.1007/BF00696758.
- McPeters, R., et al. (1998), Earth Probe Total Ozone Mapping Spectrometer (TOMS) Data Product User's Guide, *NASA/TP-1998-206895*, NASA Goddard Space Flight Cent., Greenbelt, Md.
- McPeters, R. D., G. J. Labow, and J. A. Logan (2007), Ozone climatological profiles for satellite retrieval algorithms, *J. Geophys. Res.*, *112*, D05308, doi:10.1029/2005JD006823.
- Richter, A., F. Wittrock, and J. P. Burrows (2006), SO₂ measurements with SCIAMACHY, paper presented at Atmospheric Science Conference, Eur. Space Agency Cent. for Earth Obs., Frascati, Italy, 8–12 May.
- Rodgers, C. D. (2000), *Inverse Methods for Atmospheric Sounding: Theory and Practice*, World Sci., Singapore.
- Seftor, C. J., N. C. Hsu, J. R. Herman, P. K. Bhartia, O. Torres, W. I. Rose, D. J. Schneider, and N. Krotkov (1997), Detection of volcanic ash clouds from Nimbus 7/total ozone mapping spectrometer, *J. Geophys. Res.*, *102*(D14), 16,749–16,760.
- Spurr, R. J. D. (2003), Discrete ordinate radiative transfer with rotational Raman scattering: Theory and applications, *Geophys. Res. Abstr.*, *5*, 01487.
- Taylor, S. L., R. P. Cebula, G. R. Jaross, C. Ahn, K. Yang, and P. K. Bhartia (2004), An initial application of internal validation and soft calibration techniques to preliminary OMI total ozone data, *Eos Trans. AGU*, *85*(47), Fall Meet. Suppl., Abstract A33A-0133.
- Thomas, W., T. Erbertseder, T. Ruppert, M. Van Roozendaal, J. Verdebout, D. Balis, C. Meleti, and C. Zerefos (2005), On the retrieval of volcanic sulfur dioxide emissions from GOME backscatter measurements, *J. Atmos. Chem.*, *50*, 295–320, doi:10.1007/s10874-005-5544-1.
- Vasilkov, A. P., J. Joiner, K. Yang, and P. K. Bhartia (2004), Improving total column ozone retrievals by using cloud pressures derived from Raman scattering in the UV, *Geophys. Res. Lett.*, *31*, L20109, doi:10.1029/2004GL020603.
- Veeffkind, J. P., J. F. de Haan, E. J. Brinksma, M. Kroon, and P. F. Levelt (2006), Total ozone from the Ozone Monitoring Instrument (OMI) using the DOAS technique, *IEEE Trans. Geosci. Remote Sens.*, *44*(5), 1239–1244, doi:10.1109/TGRS.2006.871204.
- Vountas, M., V. V. Rozanov, and J. P. Burrows (1998), Ring effect: Impact of rotational Raman scattering on radiative transfer in Earth's atmosphere, *J. Quant. Spectrosc. Radiat. Transfer*, *60*(6), 943–961, doi:10.1016/S0022-4073(97)00186-6.
- Wellemeyer, C. G., S. L. Taylor, C. J. Seftor, R. D. McPeters, and P. K. Bhartia (1997), A correction for the Total Ozone Mapping Spectrometer profile shape errors at high latitude, *J. Geophys. Res.*, *102*, 9029–9038.
- Wellemeyer, C. G., P. K. Bhartia, S. L. Taylor, W. Qin, and C. Ahn (2004), Version 8 Total Ozone Mapping Spectrometer (TOMS) Algorithm, paper presented at Quadrennial Ozone Symposium, Int. Ozone Comm., Athens.
- Yang, K., P. K. Bhartia, C. G. Wellemeyer, W. Qin, R. J. D. Spurr, J. P. Veeffkind, and J. F. de Haan (2004), Application of spectral fitting method to GOME and comparison with OMI-DOAS and TOMS-V8 total ozone, paper presented at Quadrennial Ozone Symposium, Int. Ozone Comm., Athens.

P. K. Bhartia, Laboratory for Atmospheres, NASA Goddard Space Flight Center, Greenbelt, MD 20771, USA.

S. A. Carn and A. J. Krueger, Joint Center for Earth Systems Technology, University of Maryland Baltimore County, Baltimore, MD 21228, USA.

N. A. Krotkov, Goddard Earth Sciences and Technology Center, University of Maryland Baltimore County, Baltimore, MD 21228, USA.

P. F. Levelt, Royal Dutch Meteorological Institute, 3730 AE, De Bilt, Netherlands.

K. Yang, NASA Goddard Space Flight Center, Mail Code 613.3, Greenbelt, MD 20771, USA. (kai.yang-1@nasa.gov)